Lawrence Berkeley National Laboratory

Title

Optimization of metal-supported solid oxide fuel cells with a focus on mass transport

Permalink

https://escholarship.org/uc/item/3v170549

Authors

Hu, Boxun

Lau, Grace

Song, Dong

et al.

Optimization of Metal-Supported Solid Oxide Fuel Cells with a Focus on Mass Transport

Boxun Hu[1], Grace Lau[1], Dong Song[2], Yosuke Fukuyama[2] and Michael C. Tucker[1*]

1. Energy Conversion Group, Lawrence Berkeley National Laboratory, Berkeley, CA 94720, USA

2. EV System Laboratory, Nissan Research Center, Nissan Motor Co., Ltd., 1 Natsushima-cho, Yokosuka, Kanagawa, 237-8523, Japan

Abstract

Performance of symmetric-architecture metal-supported solid oxide fuel cells was improved significantly by optimizing the catalyst infiltration process and metal support structure. Optimization of component structure and processing parameters was performed during tape-casting and fabrication of button cells. Mass transport of oxygen in the metal support was identified as a major limitation. To overcome this limitation, pore former loading and thickness of the metal support (130 to 250 μm) were optimized. The catalyst infiltration process was also improved by studying the impact of firing temperature (400°C to 900°C) and infiltration cycle numbers (1 to 15). The maximum power density of the optimized cell was 0.9 W cm^{-2} at 700°C using hydrogen as a fuel, a three-fold increase over the baseline cell performance. The degradation rate of optimized cells at 550°C, 600°C, and 700°C was 2%, 4.5%, and 5.5% per 100 hours, respectively. The phenomena of mass transport, catalyst coarsening, and chromium poisoning on the catalyst were analyzed by electrochemical impedance spectroscopy and scanning electron microscopy.

*mctucker@lbl.gov

Phone 1-510-486-5304

Fax 1-510-486-4260

LBNL; 1 Cyclotron Rd; MS 62-203; Berkeley CA 94720; USA

- ➢ Optimal catalyst firing temperature is 800°C.

- ➢ Optimal pore former/metal support volume ratio is 1.6:1.

- ➢ Optimal metal support thickness is approximately 195 microns.

- ➢ Optimized cell achieved 0.9 W cm^{-2} peak power at 700°C using hydrogen.

1. Introduction

Solid oxide fuel cell (SOFC) systems generate clean electricity and heat with a high energy conversion efficiency and remarkable fuel flexibility at an operating temperature range of 600°C to 1,000°C [1]. Conventional ceramic SOFCs, including electrode- or electrolyte-supported SOFCs, are usually heated up slowly (>60 minutes) to minimize damage arising from thermal stress. This limits their application, especially in the transportation sector, where rapid start-up is required. In contrast, metal-supported SOFCs (MS-SOFCs) utilize metallic supports with high thermal conductivity and ductility, thus enabling rapid startup [2] and thermal cycling [3], and providing high mechanical strength and reduced material and manufacturing costs [4, 5]. Ferritic stainless steels (SS430L, Crofer, and Fe-26 wt% Cr alloy (ITM)) are the dominant substrate materials due to their low cost, resistance to oxidation, and good electrical conductivity. Various electrolytes [6-9] and electrode catalysts [10-15] developed for SOFCs can be utilized for MS-SOFCs.

After decades of extensive research, MS-SOFC technology development is now focusing on demonstrating fuel flexibility and advancing manufacturability of MS-SOFCs for transportation and stationary power generation [5, 16, 17]. Various MS-SOFC fabrication processes, including pulsed laser deposition [6, 9], plasma spray [18, 19], sputtering [16], colloidal processes [20], or via co-sintering of the metal support and other layers produced by tape casting and other powder slurry techniques [21-23] have been reviewed by Tucker [4] and Krishnan [24]. Critical issues of metal-supported fuel cells have been analyzed by Larring and Fontaine [25]. International research teams such as Lawrence Berkeley National Laboratory (LBNL)/Nissan/Chemtronergy/UConn, DLR/Plansee/Julich/KIT, and Topsoe/Riso/DTU have demonstrated several manfacturing pathways for MS-SOFC cells, utilization of various fuels , and multi-cell stacks [26-30]. Ceres

Power has advanced their "SteelCell" technology to commercialization, with 0.5 kW L^{-1} volumetric power density reported in a stationary power configuration [20]. Pirou et al. recently reported a monolithic stack reaching a volumetric power density of 5.6 kW L^{-1} for a single-repeating unit (SRU), with a single cell power density of 0.47 W cm^{-2} at 780°C utilizing dry hydrogen (H_2) and oxygen (O_2) [31].

Symmetrical structures of porous metal support and zirconia electrode scaffold and dense electrolyte layers offer opportunities to develop a range of nanostructured electrodes by infiltration and other techniques [11, 32, 33]. LBNL previously developed a series of processing steps for the fabrication of MS-SOFCs including tape casting, lamination, and co-sintering in reducing atmosphere [34, 35]. The symmetrical cells, ranging from 5 cm^2 to 50 cm^2, remain flat after sintering at 1,350°C and endured multiple thermal cycles from 100°C to 700°C, demonstrating a path from lab scale to manufacturing scale [36]. Replacing a slow infiltration using molten nitrate salts, an alternative infiltration and "fast firing" technique with aqueous solutions improved the cell performance from 0.3 W cm^{-2} to 0.52 W cm^{-2} at 700°C and shortened the total catalyst infiltration time from 5 days to less than 2 work shifts. Despite this recent progress, a higher power density is still needed to meet the stack-level volumetric power density target of >2 kW L^{-1} for application of MS-SOFCs in consumer vehicles.

In this technical contribution, we investigate the relationship of cell structure and nanocatalyst electrode processing to performance. Mass transport is identified as a major limitation for cell performance via quantification of gas transport resistance in the anode and cathode. This limitation is addressed by optimizing the thickness and porosity of the metal supports. Process parameters including catalyst firing temperature and number of infiltration cycles are also optimized. The optimized cell shows significant improvement in cell performance.

2. Experimental Methods

2.1. Cell Fabrication and Testing

Cell preparation

Baseline cells were fabricated using a standard pore former loading (1:1 volume ratio of pore former: metal powder) and thickness (250 μm). Thinner and more porous metal supported cells were also prepared. P434L stainless steel powder (Ametek, USA) was mixed with polymer pore former beads in ratios between 1 and 2 (pore former to metal by volume), and added by ball milling for two hours. The subsequent steps for tape-casting, laser cutting, debinding, and sintering were discussed in detail previously [36]. The cells are pre-oxidized at 850°C in air for 10 hours before infiltration.

Infiltration and Fast Firing

A modified infiltration and firing method [36] was utilized for loading catalysts in the symmetrical cells. Prior to infiltration, the edge of the cell was masked with acrylic paint (Liquitex) to prevent catalyst deposition on the perimeter area. Pr-nitrate or stoichiometric mixtures of Ni-, Sm-, and Ce-nitrates (Sigma Aldrich) were mixed with Triton-X surfactant and dissolved in a small amount of water. This cathode precursor ($Pr(NO_3)_3$) was dripped onto one side of the cell, followed by application of vacuum to remove air from the cell, Then, anode catalyst precursors ($Sm(NO_3)_3$, $Ce(NO_3)_3$, $Ni(NO_3)_2$) were dripped onto the other side of the cell, followed by application of vacuum. A low temperature drying step (90°C for 15 minutes) was added to maintain the catalyst precursors inside the pores. For fast firing, the cells were directly placed in a hot furnace (600°C to 900°C) and then after slightly opening the furnace door to cool the furnace, the cell was taken out at 600°C and cooled naturally in air. Fast firing maintains the porous

structure and mitigates mass transport resistance by generating steam pressure that removes excess catalysts from the metal support. After the fast firing, excess catalyst powder from the anode and cathode were collected separately for characterization.

Cell testing

Cell testing followed a similar protocol to that published previously for electrolysis operation [37]. Platinum mesh was spot welded to each side of the cells to make electrical connections to Pt wires connected to the electrochemical testing interface. Button cells were mounted onto 410 stainless steel test rigs. Glass powder was applied as a paste (Schott GM31107 mixed with terpineol) by syringe to the edges of the cells and heated to 90°C at 10°C min^{-1}, then to 200°C at a ramp rate of 2°C min^{-1}, and finally to 700°C at a ramp rate of 10°C min^{-1} with a dwell time of one hour. The cell supported on a test rig was placed in a two-inch diameter alumina tube (with one end open). The open end was stuffed with insulating alumina fibers (Zircar). The anode was then flushed with nitrogen before introducing 150 cm^3 min^{-1} humidified hydrogen (3% moisture). The cathode was exposed to either ambient air, or air flowing at 500 cm^3 min^{-1}. Open circuit voltage (OCV), electrochemical impedance spectroscopy (EIS) at OCV and 0.7 V, and cell performance (IV-PI and I-t) were assessed with a multichannel potentiostat with current boosters (Biologic VMP3 with 10 A boosters). For stability tests, cells were pre-coarsened at 750°C for 4 h before operation.

2.2 Characterization

X-ray diffraction

High temperature-XRD (HT-XRD) was performed using an automated multipurpose X-ray diffractometer equipped with an Anton Paar high-temperature oven chamber and SmartLab Studio

II software. The samples of electrode catalysts (same as infiltration solution) were dried at 120°C for 1 hour and pre-calcined in a box furnace at 400°C to avoid harmful gas being evolved in the HT-XRD. The powder was heated from 400°C up to 900°C at a ramp rate of 10°C with a dwell time of 10 minutes at each measured temperature. The HT-XRD scanned the sample with a speed of 5°C min^{-1} at a step of 0.01° and 2Θ range from 20 degrees to 80 degrees. Crystal structure of the excess catalysts from infiltrated MS-SOFCs after firing in an oven was characterized by x-ray diffraction (XRD, Bruker D2 Phaser), with a scanning speed of 5° min^{-1} at a step of 0.02°. For the crystallite size analysis of the excess catalyst powders, LaB_6 (Alfa Aesar) was utilized as a size/strain standard to calibrate instrumental broadening of diffraction peaks.

Scanning Electron Microscopy - Energy Dispersive X-ray Spectroscopy

Cells were mounted in epoxy, cut, and polished to prepare for the scanning electron microscope (SEM). Field emission scanning electron microscopy (FESEM) images were collected using a Zeiss Gemini Ultra-55 instrument with an in-lens and quadrant backscatter detector, at a voltage of 20 kV. An energy dispersive X-ray (EDX) detector was used for element analysis, with a beam energy of 20 kV.
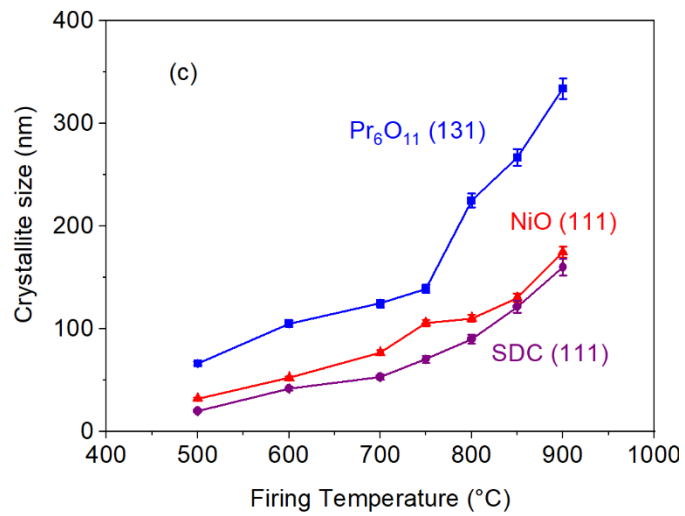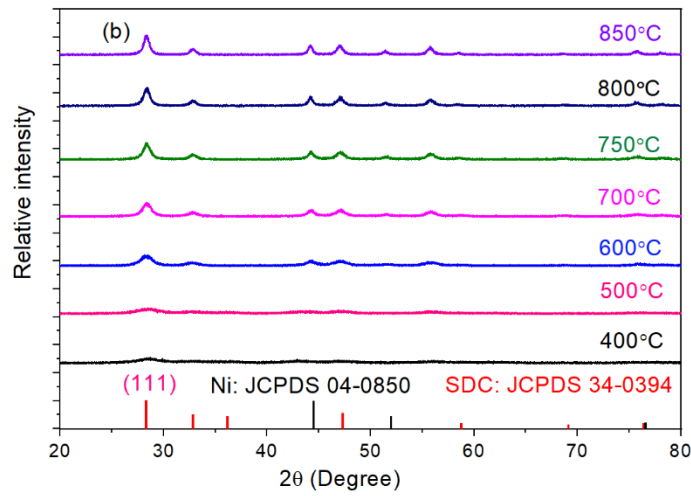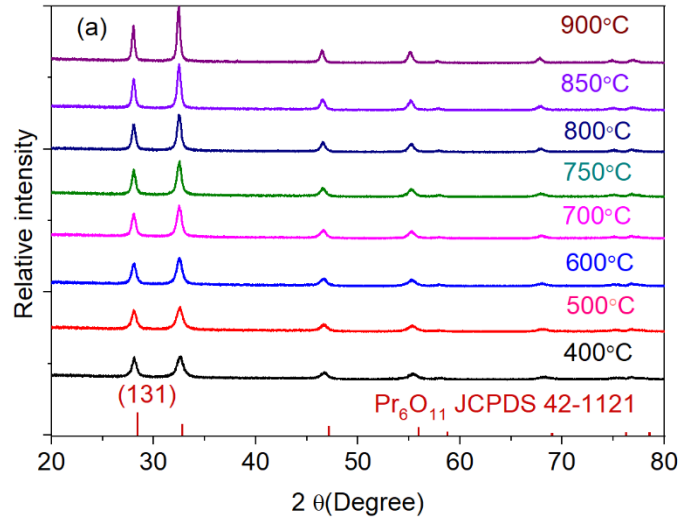
3. Results and Discussion

Cell optimization used our previous symmetric cell structure and catalyst processing as a baseline [38]. Previously, Pr_6O_{11} cathode catalyst and 40 vol% Ni-60 vol% $Sm_{0.20}Ce_{0.80}O_{2-\delta}$ (SDCN) anode catalysts were infiltrated and fast fired at a temperature of up to 600°C [36]. The metal support of the previous standard cell was approximately 250 μm thick, and 1:1 volume ratio of pore former to metal support was added. These features are used here as the baseline for cell performance comparison. The structure and thickness of the electrolyte and electrode backbone

were not adjusted in the present work. The cell optimization was divided into two stages. The first stage was catalyst optimization, including the determination of the best firing temperature and number of infiltration cycles. After the catalyst optimization, mass transport was identified as a major limitation. Structural optimization of the metal support, including determination of the optimal pore former loading and metal support thickness, was performed to improve mass transport.

3.1 Catalyst Structure and Crystallite Size

High temperature XRD of the cathode (Pr_6O_{11}) and anode (SDCN) catalysts determined the phase stability and catalyst size evolution at a temperature range of 400°C to 900°C (Figure 1). A single phase of Pr_6O_{11} (JCPDS # 42-1121) was formed at 400°C or lower, and persisted up to 900°C (Figure 1a). For the SDCN catalyst, amorphous NiO and Sm-doped CeO_2 (SDC) phases were formed after firing in air at 400°C, and crystalline SDC (JCPDS #34-0394) and Ni (JCPDS # 04-0850) catalysts were formed by 600°C in 4% H_2/N_2 (Figure 1b). The intensity of the XRD peaks increased with firing temperature for all catalyst types, as the crystallinity increased. The calculated crystallite size of the Pr_6O_{11} and NiO-SDC catalysts increased with firing temperature (Figure 1c and Table S1). When the infiltrated cell was fired at 800°C, the average crystallite size calculated with the Scherrer Equation for Pr_6O_{11} (131), $SmCeO_2$ (111), and NiO (111) were 225.0 nm, 90.1 nm, and 110.3 nm, respectively. The calculated crystallite sizes are consistent with the particle feature size observed in SEM images (Figure S1).

(a)

900°C
850°C
800°C
750°C
700°C
600°C
500°C
400°C

(131) Pr₆O₁₁ JCPDS 42-1121

(b)

850°C
800°C
750°C
700°C
600°C
500°C
400°C

(111) Ni: JCPDS 04-0850 SDC: JCPDS 34-0394

(c)

Pr₆O₁₁ (131)

NiO (111)

SDC (111)

Figure 1. Catalyst phase formation. HT-XRD patterns for a: Pr_6O_{11} catalyst heated in compressed air, and b: SDCN catalyst heated in 4% H_2/N_2. c: Crystallite sizes of excess catalysts during fast firing in air calculated by XRD data (not shown) and the Scherrer Equation [39].

## 3.2 Catalyst processing optimization

Electrode catalyst loading was controlled by the number of infiltration cycles. Cells prepared with 3 to 15 infiltration cycles were tested, and the highest performance was achieved for 10 cycles (Figure S2), consistent with the limited optimization done previously [36]. Increasing the infiltration cycles from 3x to 10x continuously reduced the ohmic resistance. Further increase of infiltration cycle to 13x and 15x resulted in higher polarization resistance due to mass transport limitation.

MS-SOFCs were tested with electrode catalysts fast fired over a wide firing temperature range of 350°C to 900°C (Figure 2 a and b). The best firing temperature was determined to be 800°C, at which the maximum power (Pmax) was 0.61 W cm^{-2}. Pmax was not linear with temperature, and performance dropped in the temperature range of 600°C to 750°C. Six identical cells with catalyst firing temperatures of 700°C and 750°C were tested and confirmed that the cell performance significantly dropped in this range. It appears that this non-linear behavior results from the interplay of several factors. Vshivkova et al. reported that the electrical conductivity of the Pr_6O_{11} films on Al_2O_3 jumped at 624°C and 690°C, and the DSC heating curve showed a peak at 740°C, suggesting decomposition or phase change of Pr_6O_{11} in this temperature range [40]. However, the HT-XRD here did not detect any secondary phase in the range 600 to 750°C (Figure 1a). With increasing firing temperature, catalyst/ScSZ contact improves and large crystallites are formed (especially above 700°C, Figure 1c), which is expected to reduce the ohmic resistance of the electrodes. Simultaneously, the surface area of the electrode catalyst decreases with an increase of

firing temperature. Cr evaporation is temperature-dependent and migration from the metal support to the cathode catalyst during firing is known to impact performance [41]. Above 800°C, the cell performance dropped with an increase of catalyst crystallite size (Table S1) and Cr atom percentage in the cathode (Table S2). Stainless steel oxidation is also greatly enhanced above 800°C [42]. The optimal temperature of 800°C is the result of complex interaction between the above factors.

Cell stability is quite sensitive to catalyst firing temperature. Representative cells fired at 350°C, 500°C, and 800°C degraded at 52%, 40%, and 13%, respectively, in a 100-hour test (Figure 2c). Results for all temperatures are summarized in Figure 2b. Cells fired at low temperatures (below 700°C) showed fast degradation rates (>20%) because nano-size catalysts (<50 nm, Figure 1c) are prone to particle coarsening, which was identified previously as a primary degradation mode [35, 41]. The cells fired at 800°C and above, where the catalysts have a moderate crystallite size range of 90 to 330 nm (Table S1), showed a high initial current density and a high stability. Cell stability is impacted by the catalyst crystallite size, current density, and Cr migration from the metal support. The cell stability shows a complex temperature-dependence, reflecting a combined effect of these factors.

Based on the above results, 10 cycles of catalyst infiltration via fast firing at 800°C was chosen as the standard processing for all further cell optimization and testing in the following sections.
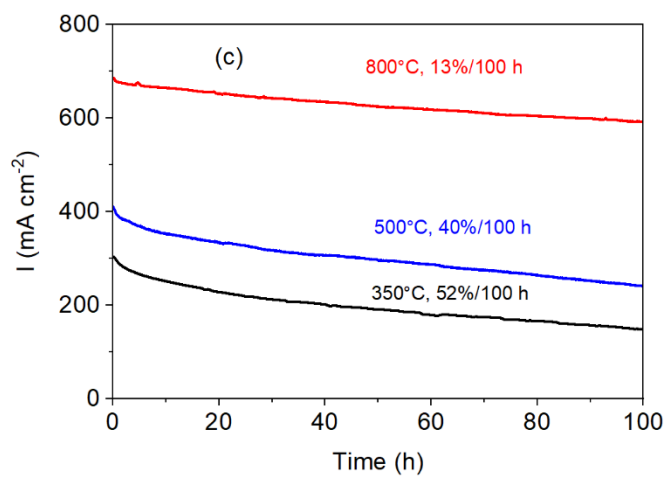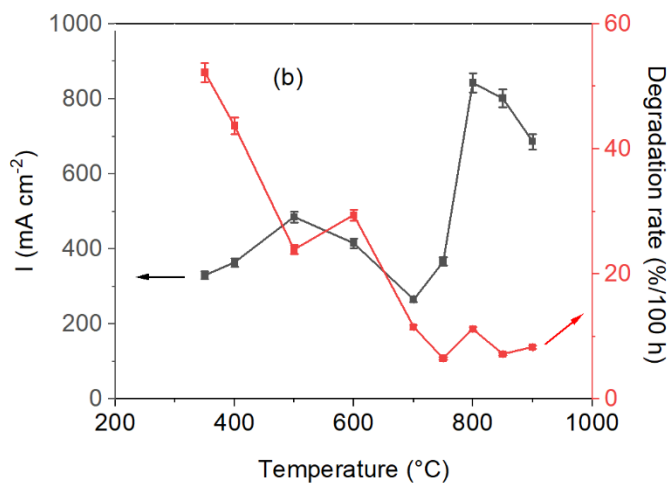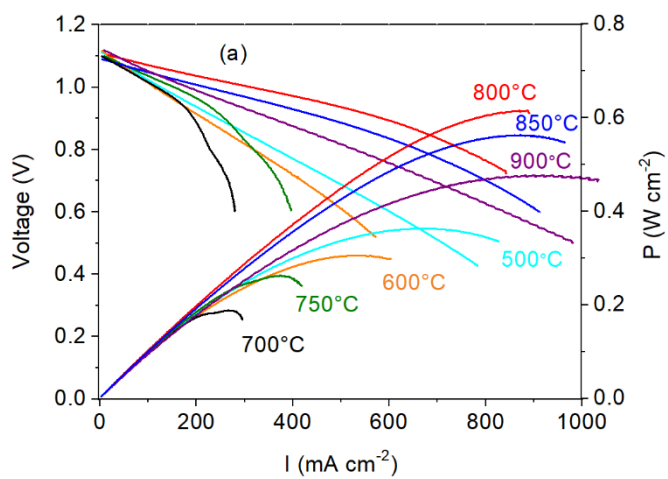
Figure 2. Impact of catalyst firing temperature on MS-SOFC performance and stability. a: Polarization curves. b: Current density and degradation rate versus firing temperature. c: Potentiostatic durability for select cells at 0.7 V and 700°C with ambient air. Standard cells with a metal support thickness of 250 μm and 10x infiltration.

3.3 Mass Transport Limitation

After catalyst optimization, oxygen mass transport was the primary performance limitation. Pmax with oxygen was 2.1 times higher than Pmax with air, and the I-V curve for air was bent towards a limiting current around 1 A cm^{-2}, indicating the cell performance was limited by concentration polarization on the cathode side (Figure 3a). To quantify the mass transport resistance for the cathode and anode independently, a method based on enhancing concentration polarization on each side separately was utilized [43]. Briefly, the oxygen or hydrogen concentration in the feed gas is reduced, and the limiting current is determined, allowing the gas transport resistance to be calculated (Figure 3b,c). Further details can be found in the supporting information. The same limiting current is observed for 30% to 100% H_2 (Figure 3c) and it is indentical to the 21% O_2 (air) case in Figure 3b. This indicates that oxygen transport is the cause of the limiting current for these higher H_2 concentrations. However, in the case of 15% H_2, the anode limiting current dominates, so the anode gas transport resistance was quantfied from the 15% H_2 data. Polarization curves for 2% O_2 and 15% H_2 were extrapolated to 0 V to estimate the limiting currents, which were used to calculate the oxygen (R_{O2}) and hydrogen (R_{H2}) transport resistances to be 123.9 sec m^{-1} and 44.8 sec m^{-1}, respectively. Clearly, the high R_{O2} dominates the concentration polarization behavior when using air.

This quantification of the gas transport resistance suggested that it is necessary to optimize the thickness and pore structure of the metal support and electrode backbone to reduce R_{O2}. To

determine if the metal support or electrode dominated R_{O2}, cells with a double thickness of metal support or a double thickness of electrode were tested and compared to the baseline cell (Figure S4). To maintain the symmetric cell architecture, the same metal support and electrode structures were used on both sides. Doubling the metal support thickness reduced I_{lim} from approximately 1 to 0.75 A cm^{-2}, and increased the EIS polarization resistance from 0.42 to 0.73 Ω cm^2. In contrast, doubling the electrode thickness did not increase the polarization resistance and I_{lim} was not observed, because the thick electrode increased ohmic impedance yielding an ohmic-dominated polarization curve that did not extend above 0.7 A cm^{-2}. These EIS and VI-PI results indicate that the mass transport limitation is dominated by the metal support. Therefore, we focused on optimizing porosity and thickness of the metal support to reduce R_{O2}.
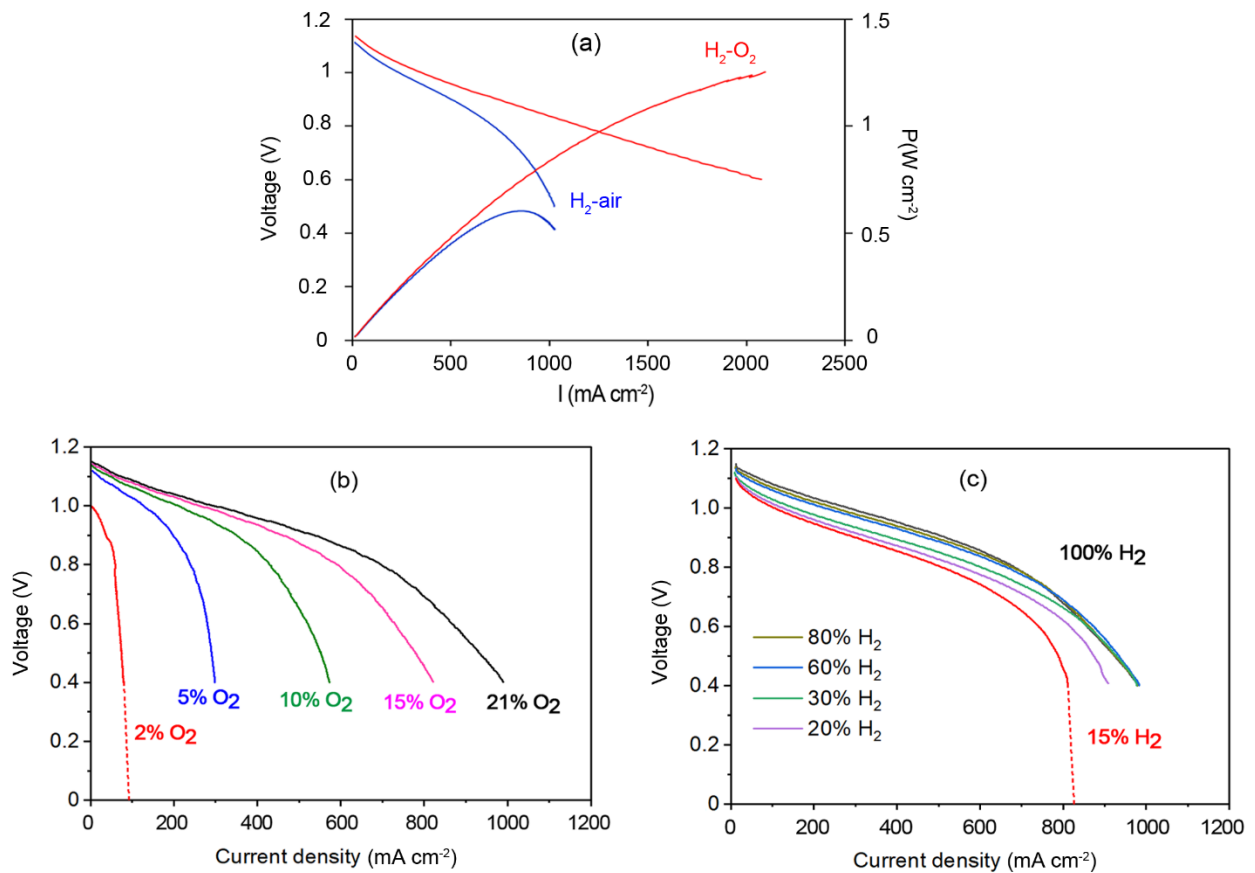
Figure 3. Identifying oxygen mass transport as the dominant limitation to cell performance at 700°C. (a) Polarization behavior of a MS-SOFC utilizing air (blue) or oxygen (red); catalysts were infiltrated 10 times and fired at 800°C. Polarization curves for dilution of (c) oxygen (with 97% H_2/3% H_2O at the anode) and (d) hydrogen (with air at the cathode).

3.4 Metal Support Optimization

Increasing porosity is one approach for mitigating the mass transport limitation in the metal support. Adding additional pore former in the metal support slurry before tape casting increased the porosity, as seen in the SEM images (Figure 4). However, the best performance is observed for 1.6:1 pore former/metal support volume ratio. For this cell, almost 2 A cm^{-2} is achieved without significant limiting current behavior. With 2:1 pore former/metal support volume ratio, the additional porosity appears to interfere with electronic contact at the metal support/electrode interface due to large gaps between adjacent metal contact points (Figure 4d), and ohmic resistance increased from 0.24 Ω cm^2 for 1.6:1 pore former/MS volume ratio to 0.45 Ω cm^2 for 2:1 pore former/MS volume ratio (Figure S5). Based on these results, 1.6:1 pore former/metal support volume ration was chosen for further studies.
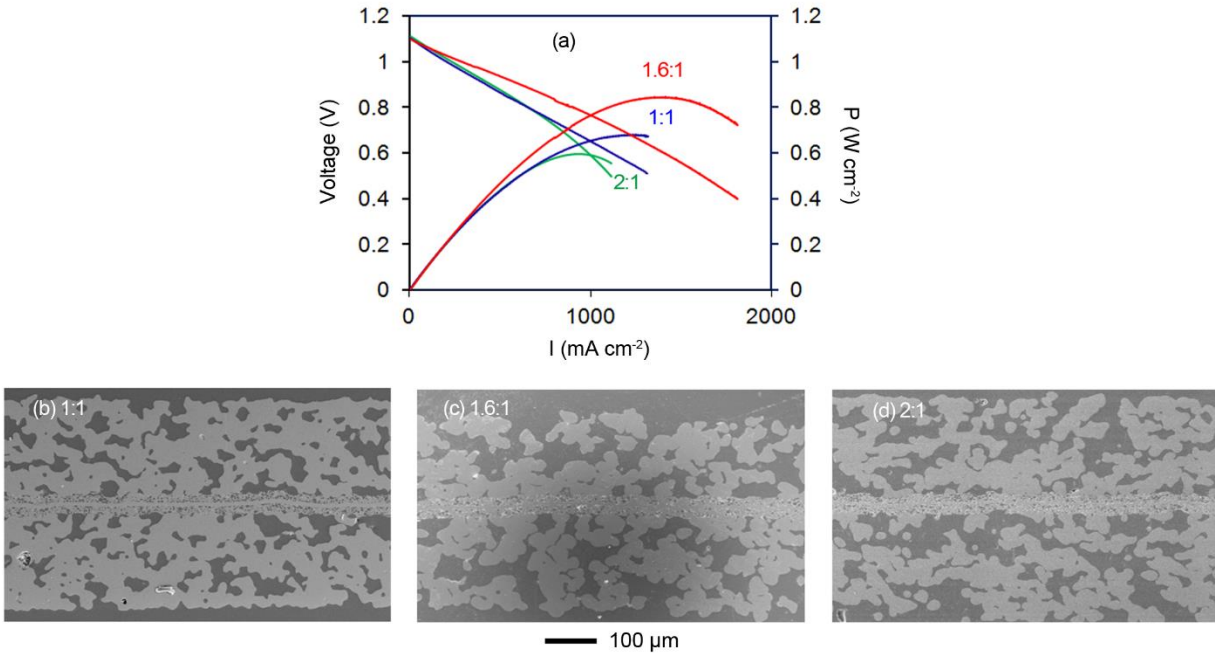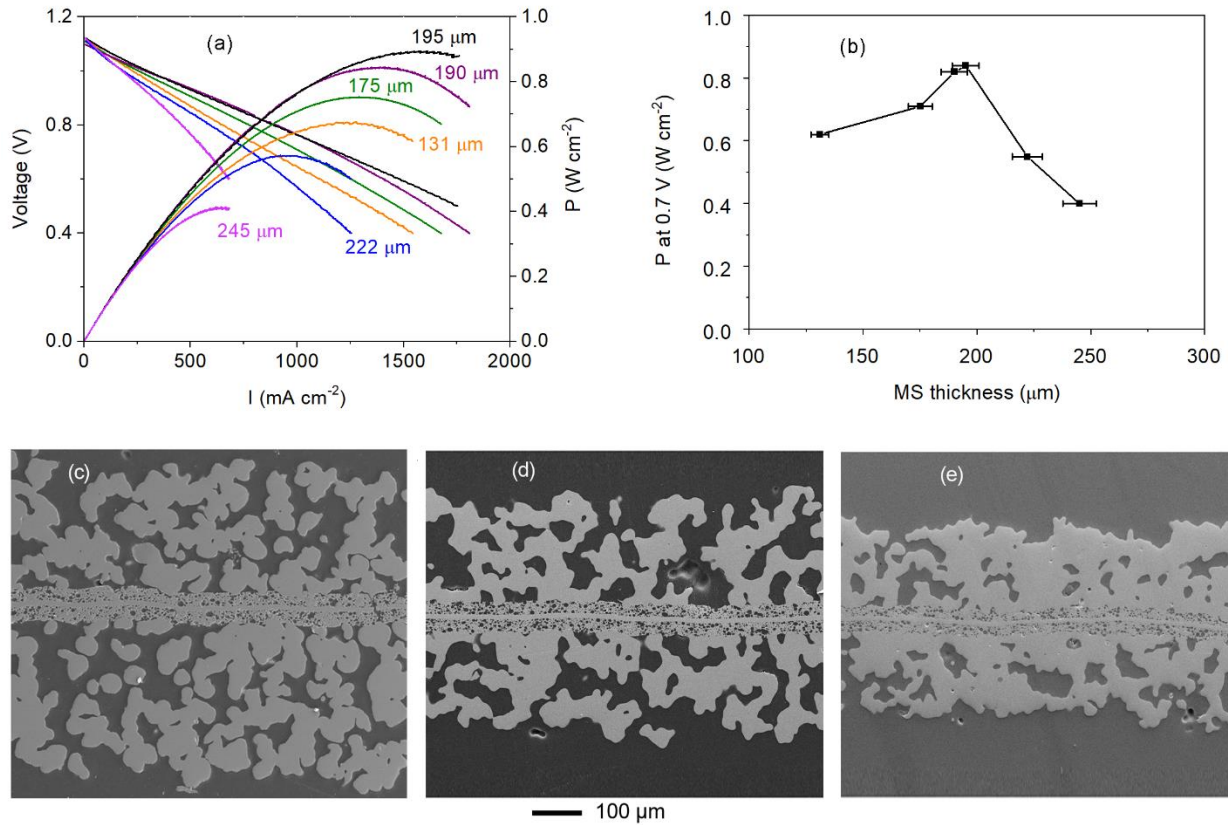
Figure 4. Impact of metal support porosity on MS-SOFC performance at 700°C. a: Polarization behavior of MS-SOFCs with various pore former loadings. b, c, and d: SEM cross section images of MS-SOFC structures (no catalysts added) with pore former loadings of (b) 1:1, (c) 1.6:1, and (d) 2:1 pore former/metal support volume ratio.

Reducing the metal support thickness is another approach to decrease mass transport resistance. MS-SOFCs with a wide range of metal support thickness were prepared by adjusting the casting gap height during tape casting (Figure 5). For the baseline metal support (245 μm thick), a low Pmax of 0.4 W cm^{-2} was obtained, due to large mass transportation resistance (Figure 5 a and c). With metal support thickness decreasing to 195 μm, the performance increased to Pmax of 0.9 W cm^{-2} (Figures 5b, d and Table S4). Further reducing the metal support thickness led to over-sintering of the metal support (Figure 5c), and decreased the cell performance due to collapse of the pore structure. This densification of the metal support below a threshold thickness was also

observed in previous MS-SOFC work [28]. Based on these results, the best metal support thickness of 195 μm was chosen for further studies.


Figure 5. The impact of metal support thickness on MS-SOFC performance at 700°C.a: Polarization behavior of MS-SOFCs with various thickness of metal supports and 1.6:1 pore former/metal support volume ratio. b: Dependence of power density at 0.7 V on metal support thickness. SEM cross-section images of MS-SOFC structures (no catalysts added) with metal support thicknesses of (c) 245 μm, (d) 195 μm, and (e) 131 μm. SEM images for other thicknesses are available in the supporting information (Figure S6).

3.5 Cell Performance After Optimization

Optimization of the catalyst processing and metal support structure significantly improved MS-SOFC cell performance (Figure 6). After catalyst optimization and properly selecting the firing temperature, the Pmax with air and hydrogen fuel was improved from 0.31 W cm^{-2} (baseline cell) to 0.56 W cm^{-2}. After the metal support structure optimization, the Pmax was further improved to 0.9 W cm^{-2} at a cell voltage of 0.6 V. The EIS spectra show that the ohmic resistance was reduced from 0.46 Ω cm^2 for the baseline cell to 0.14 Ω cm^2 after catalyst optimization, and the polarization resistance was slightly reduced from 0.84 Ω cm^2 to 0.67 Ω cm^2. The catalysts fired at higher temperature (800°C) kept good contact with catalyst supports (ScSZ). The catalysts with larger crystallite sizes (Table S1) have less grain boundary, better particle-particle contact, and reduce the ohmic resistance. Sufficient (but not excess) catalyst loading provided by the best number of infiltration cycles (10x) maintains the porous structure and reduced the concentration polarization resistance.

The metal support structure optimization further reduced the polarization resistances of the cell from 0.67 Ω cm^2 to 0.42 Ω cm^2. These improvements arise from reduced mass transport limitation and possibly improved infiltration through the support into the electrode, and are due to optimization of the metal support pore structure and thickness. The R_{O2} of the optimized cell was quantified using the method described in Section 3.3, and improved approximately three-fold to 44.2 sec m^{-1} (Figure S3). This confirms that the cell optimization effectively reduced the mass transport resistance of oxygen. The ohmic resistance of the optimized structure cell was slightly increased due to an increase of pore former in the metal support and a reduction of metal support/electrode contact, as discussed above in Section 3.4. The best pore former/metal ratio reflects the needs of mass transport and good metal support/electrode contact.
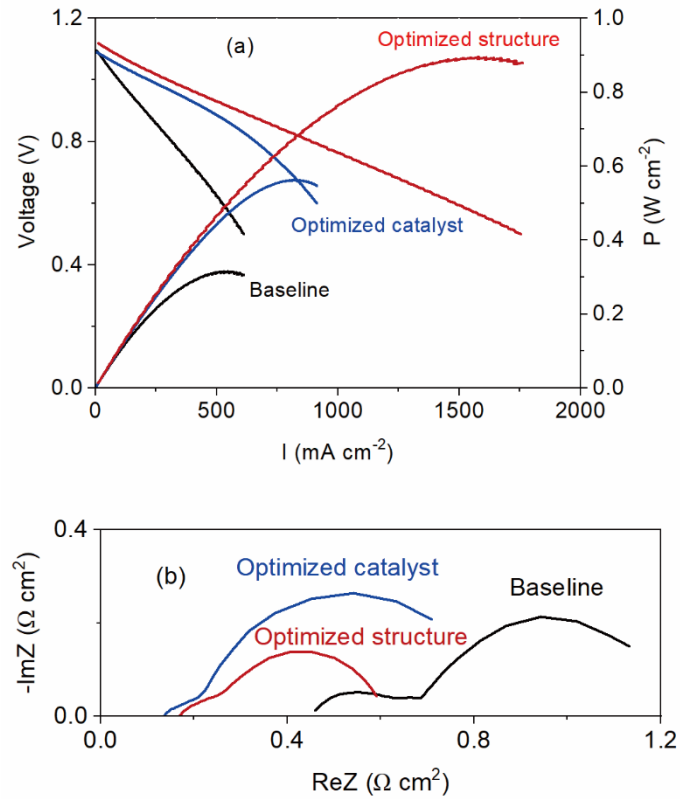
Figure 6. Summary of optimization improvements. Comparisons of MS-SOFC (a) polarization and (b) EIS spectra at 700°C, at three development stages. The baseline cell had metal support thickness around 250 μm, with 1:1 pore former/metal support volume ratio, and was infiltrated 10x and fired at 600°C after infiltration. The cell with optimized catalyst was similar except that the catalysts were fast fired at 800°C. The cell with optimized structure had metal support thickness of 195 μm, with 1.6:1 pore former/metal support volume ratio, with catalysts infiltrated 10x and fast fired at 800°C.

3.6 Cell Stability

Short-term stability of the optimized cells was assessed in the operating temperature range of 550°C to 700°C using air and hydrogen fuel (Figure 7). Holding the cell at OCV at 750°C for 4 h before operation pre-coarsened the catalysts, and thus improved the cell stability but decreased the initial cell performance [41]. The cell degradation rates are 2%, 4.5%, and 5.5% per 100 hours for 550°C, 600°C, and 700°C, respectively. The degradation rate increases with increasing operating temperature. This is expected, as Cr deposition and catalyst coarsening are the major degradation phenomena identified previously [41], and both are temperature-dependent. The current density also increases with increasing temperature, and higher current density is associated with faster degradation [44]. The improved performance achieved via cell optimization enables operation at lower temperature, which is expected to increase cell longevity. Long-term operation followed by detailed post-mortem analysis and improvement of the durability is the focus of ongoing work.
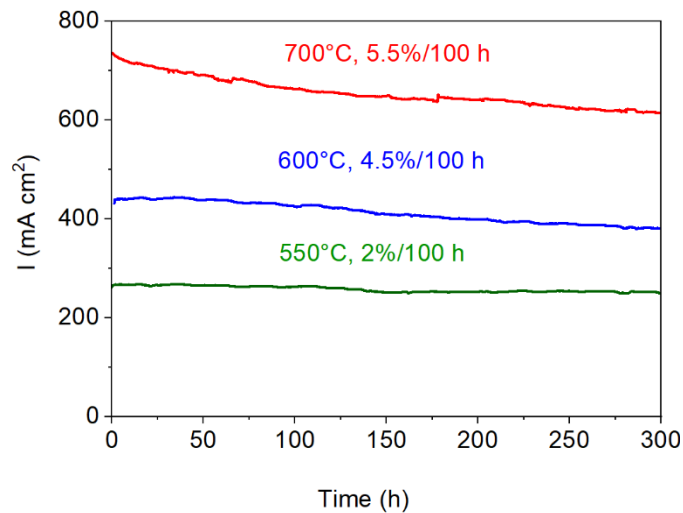
Figure 7. Impact of operating temperature on cell stability. Potentiostatic operation of the optimized MS-SOFCs at 550°C, 600°C, and 700°C, with a cell voltage of 0.7 V, 150 sccm 97% H_2/3% H_2O fuel flow for the anode and 500 cm^3 min^{-1} dry air flow for the cathode.

4. **Conclusions**

The symmetric-structure MS-SOFC was optimized by proper selection of the number of infiltration cycles, catalyst firing temperature, pore former loading, and metal support thickness. The best performance for baseline cells was achieved with 10 catalyst infiltration cycles. The catalyst firing temperature greatly affected the cell performance. The best firing temperature for the infiltrated cells was 800°C, utilizing a fast firing process. The symmetric MS-SOFC architecture endured very fast thermal processing and direct firing at 800°C, thereby shortening the cell fabrication time. The initial baseline cell with a 250 µm metal support showed a large oxygen concentration polarization associated with low porosity in the thick cathode-side metal support. The resulting mass transport limitation severely restricted performance, and was mitigated by increasing the porosity and decreasing the thickness of the metal support. MS-SOFCs with three different pore former loadings were tested, and the best was found to be 1.6:1 pore former/metal support volume ratio. MS-SOFCs with a metal support thickness ranging from 131 to 250 µm were tested with optimized catalysts. The optimal thickness of the metal support is about 190 to 195 µm. For thinner supports, over-densification of the metal reduced cell performance. After this optimization, the initial cell peak power was improved from 0.31 W cm^{-2} to 0.9 W cm^{-2}, providing a high-power single cell for MS-SOFC stacks and power systems for transportation applications. The dramatic improvement of cell performance enables operation at relatively low temperature, which is anticipated to improve system lifetime and cost. The optimized cell shows good stability at a low operating temperature of 550°C.

References

[1] K. Eguchi, H. Kojo, T. Takeguchi, R. Kikuchi, K. Sasaki, Solid State Ion., 152-153 (2002) 411-416.

[2] M.C. Tucker, A.S. Ying, Int. J. Hydrogen Energy, 42 (2017) 24426-24434.

[3] M.C. Tucker, J. Power Sources, 395 (2018) 314-317.

[4] M.C. Tucker, J. Power Sources, 195 (2010) 4570-4582.

[5] P. Blennow, J. Hjelm, T. Klemensø, S. Ramousse, A. Kromp, A. Leonide, A. Weber, J. Power Sources, 196 (2011) 7117-7125.

[6] M. Stange, E. Stefan, C. Denonville, Y. Larring, P.M. Rørvik, R. Haugsrud, Inter. J. Hydrogen Energy, 42 (2017) 13454-13462.

[7] Y. Wang, Y. Song, J. Liu, K. Yang, X. Lin, Z. Yang, F. Ciucci, Adv. Energy Sustainability Res., 3 (2021) 2100171.

[8] C. Hwang, T. Hwang, C. Tsai, C. Chang, S. Yang, M. Wu, C. Fu, Ceram. Int., 43 (2017) 591-597.

[9] E. Stefan, M. Stange, C. Denonville, Y. Larring, N. Hildenbrand, T. Norby, R. Haugsrud, J. Mater. Sci., 52 (2017) 6486-6497.

[10] H. Tang, Z. Gong, Y. Wu, Z. Jin, W. Liu, Int. J. Hydrogen Energy, 43 (2018) 19749-19756.

[11] Y. Zhou, C. Yuan, T. Chen, X. Meng, X. Ye, J. Li, S. Wang, Z. Zhan, J. Power Sources, 267 (2014) 117-122.

[12] M. Khoshkalam, M.A. Faghihi-Sani, X. Tong, M. Chen, P.V. Hendriksen, J. Electrochem. Soc., 167 (2020) 24505.

[13] Z. Gao, X. Ding, D. Ding, L. Ding, S. Zhang, G. Yuan, Int. J. Hydrogen Energy, 43 (2018) 8953-8961.

[14] H. Kang, S. Grewal, H. Li, M.H. Lee, J. Electrochem. Soc., 166 (2019) 255-263.

[15] A. Nenning, C. Bischof, J. Fleig, M. Bram, A.K. Opitz, Energies, 13 (2020) 987.

[16] D. Udomsilp, J. Rechberger, R. Neubauer, C. Bischof, F. Thaler, W. Schafbauer, N.H. Menzler, L.G.J. de Haart, A. Nenning, A.K. Opitz, O. Guillon, M. Bram, Cell Rep. Phys. Sci., 1 (2020) 100072.

[17] R.P. Dowd, S. Lee, Y. Fan, K. Gerdes, Int. J. Hydrogen Energy, 41 (2016) 14971-14981.

[18] T. Franco, K. Schibinger, Z. Ilhan, G. Schiller, A. Venskutonis, ECS Trans., 7 (2007) 771-780.

[19] R. Hui, Z. Wang, O. Kesler, L. Rose, J. Jankovic, S. Yick, R. Maric, D. Ghosh, J. Power Sources, 170 (2007) 308-323.

[20] R.T. Leah, A. Bone, A. Selcuk, M. Rahman, A. Clare, M. Lankin, F. Felix, S. Mukerjee, M. Selby, ECS Trans., 91 (2019) 51-61.

[21] P. Blennow, J. Hjelm, T. Klemensø, A.s. Persson, K. Brodersen, A. Srivastava, H. Frandsen, M. Lundberg, S. Ramousse, M. Mogensen, ECS Trans., 25 (2009) 701-710.

[22] T. Chen, Y. Zhou, M. Liu, C. Yuan, X. Ye, Z. Zhan, S. Wang, Electrochem. Commun., 54 (2015) 23-27.

[23] Y. Zhou, C. Yuan, T. Chen, X. Meng, X. Ye, J. Li, S. Wang, Z. Zhan, J. Power Sources, 267 (2014) 117-122.

[24] V.V. Krishnan, Wiley Interdiscip. Rev. Energy Environ., 6 (2017) 246.

[25] Y. Larring, M.-L. Fontaine, Critical Issues of Metal-Supported Fuel Cell, in: P.C. John T.S. Irvine (Ed.) Solid Oxide Fuels Cells: Facts and Figures, 2013, pp. 71-93.

[26] E. Dogdibegovic, Y. Fukuyama, M.C. Tucker, J. Power Sources, 449 (2020) 227598.

[27] B.R. Sudireddy, J. Nielsen, Å.H. Persson, K. Thydén, K. Brodersen, S. Ramousse, D. Neagu, E. Stefan, J.T.S. Irvine, H. Geisler, A. Weber, G. Reiss, R. Schauperl, J. Rechberger, J. Froitzheim, R. Sachitanand, H. Falk-Windisch, J.E. Svensson, M.W. Lundberg, R. Berger, J. Westlinder, S. Hornauer, T. Kiefer, Fuel Cells, 17 (2017) 508-516.

[28] J. Nielsen, Å.H. Persson, T.T. Muhl, K. Brodersen, J. Electrochem. Soc., 165 (2018) 90-96.

[29] M.M. Welander, B. Hu, M.C. Tucker, Inter. J. Hydrogen Energy, 47 (2022) 11261-11269.

[30] J.O. Christensen, B.R. Sudireddy, A. Hagen, ECS Trans., 103 (2021) 713-724.

[31] S. Pirou, B. Talic, K. Brodersen, A. Hauch, H.L. Frandsen, T.L. Skafte, A.H. Persson, J.V.T. Hogh, H. Henriksen, M. Navasa, X.Y. Miao, X. Georgolamprou, S.P.V. Foghmoes, P.V. Hendriksen, E.R. Nielsen, J. Nielsen, A.C. Wulff, S.H. Jensen, P. Zielke, A. Hagen, Nat. Commun., 13 (2022) 1263.

[32] A.R. Hanifi, S. Paulson, A. Torabi, A. Shinbine, M.C. Tucker, V. Birss, T.H. Etsell, P. Sarkar, J. Power Sources, 266 (2014) 121-131.

[33] M.C. Tucker, G.Y. Lau, C.P. Jacobson, L.C. DeJonghe, S.J. Visco, J. Power Sources, 171 (2007) 477-482.

[34] M.C. Tucker, B. Carreon, J. Charyasatit, K. Langston, C. Taylor, J. Manjarrez, N. Burton, M. LaBarbera, C.P. Jacobson, ECS Trans., 57 (2013) 503-509.

[35] M.C. Tucker, J. Power Sources, 369 (2017) 6-12.

[36] E. Dogdibegovic, Y. Cheng, F. Shen, R. Wang, B. Hu, M.C. Tucker, J. Power Sources, 489 (2021) 229439.

[37] F. Shen, M.M. Welander, M.C. Tucker, Front. in Energy Res., 10 (2022) 817981.

[38] E. Dogdibegovic, R. Wang, G.Y. Lau, M.C. Tucker, J. Power Sources, 410-411 (2019) 91-98.

[39] B. Hu, C. Chen, S. J. Frueh, L. Jin, R. Joesten, S.L. Suib, J. Phys. Chem. C, 114 (2010) 9835–9844.

[40] A.I. Vshivkova, V.P. Gorelov, A.V. Kuz'min, S.V. Plaksin, A.A. Pankratov, T.V. Yaroslavtseva, Inorg. Mater., 51 (2015) 1168-1176.

[41] E. Dogdibegovic, R. Wang, G.Y. Lau, A. Karimaghaloo, M.H. Lee, M.C. Tucker, J. Power Sources, 437 (2019) 226935.

[42] D. Koszelow, M. Makowska, F. Marone, J. Karczewski, P. Jasiński, S. Molin, Corros. Sci., 189 (2021) 109589.

[43] Y. Fukuyama, T. Shiomi, T. Kotaka, Y. Tabuchi, Electrochim. Acta, 117 (2014) 367-378.

[44] M.Z. Khan, R.-H. Song, A. Hussain, S.-B. Lee, T.-H. Lim, J.-E. Hong, J. Eur. Ceram. Soc., 40 (2020) 1407-1417.